

See discussions, stats, and author profiles for this publication at: <https://www.researchgate.net/publication/329390819>

A reference model for airborne wind energy systems for optimization and control

Preprint · December 2018

CITATIONS

0

READS

97

4 authors, including:



Elena Malz

Chalmers University of Technology

5 PUBLICATIONS 1 CITATION

[SEE PROFILE](#)



Jonas Koenemann

University of Freiburg

8 PUBLICATIONS 163 CITATIONS

[SEE PROFILE](#)



Sebastien Gros

Norwegian University of Science and Technology

92 PUBLICATIONS 690 CITATIONS

[SEE PROFILE](#)

Some of the authors of this publication are also working on these related projects:



Eco4Wind [View project](#)



AWESCO - Airborne Wind Energy System Modelling, Control and Optimisation [View project](#)

A reference model for airborne wind energy systems for optimization and control

E. C. Malz^{a,*}, J. Koenemann^b, S. Sieberling^c, S. Gros^d

^a*Department of Electrical Engineering, Chalmers University of Technology, Göteborg, Sweden*

^b*Department of Microsystems Engineering (IMTEK), University of Freiburg, Freiburg, Germany*

^c*Ampyx Power, The Hague, Netherlands*

^d*Department of Engineering Cybernetics, Norwegian University of Science and Technology (NTNU), Trondheim, Norway*

Abstract

Airborne Wind Energy (AWE) is a promising new technology, and attracts a growing academic and industrial attention. Important research efforts have been deployed to develop prototypes in order to test the technology, generate control algorithms and optimize the efficiency of AWE systems. By today, a large set of control and optimization methods is available for AWE systems. However, because no validated reference model is available, there is a lack of benchmark for these methods. In this paper, we provide a reference model for pumping mode AWE systems based on rigid wings. The model describes the flight dynamics of a tethered 6 degrees of freedom (DOF) rigid body aircraft in form of differential-algebraic equations, based on Lagrange dynamics. With the help of least squares fitting the model is assessed using real flight data from the Ampyx Power prototype AP2. The model equations are smooth and have a low symbolic complexity, so as to make the model ideal for optimization and control. The information given in this paper aims at providing AWE researchers with a model that has been validated against flight data and that is well suited for trajectory and power output simulation and optimization.

Keywords: wind energy, airborne wind energy, modeling, validation

1. Introduction

In the recent years Airborne Wind Energy (AWE) has attracted a growing interest as a novel wind power technology. AWE harvests wind energy by means of a tethered aircraft flying in a crosswind pattern creating large lift forces. Compared to traditional wind energy technologies, greater altitude can be reached by AWE systems, hence accessing stronger and steadier winds. Another promising advantage of AWE is the reduction of construction material as AWE requires significantly less structure than wind turbines [1]. The two most promising approaches to AWE are the pumping and drag mode [1]. Drag-mode AWE systems are based on rigid wings with onboard turbines generating electrical energy by fast cross wind flights and transmitting the energy to the

*Corresponding author

Email addresses: elenama@chalmers.se (E. C. Malz), Jonas.Koenemann@imtek.de (J. Koenemann), soeren@ampyxpower.com (S. Sieberling), sebastien.gros@ntnu.no (S. Gros)

10 ground via the tether. Pumping-mode AWE systems generate mechanical energy by reeling out a
11 tethered wing from a winch and retract using a fraction of the produced energy.

12 There exist several companies building prototypes at different scales of both pumping and drag-
13 mode AWE systems [2–4] and the research in AWE control, power maximization and component
14 optimization is increasing [5]. Currently, the technology has not yet reached a commercial de-
15 ployment and there are many unknowns regarding its viability, pertaining e.g. power availability
16 throughout the year compared to traditional wind turbines, maintenance costs, reliability, safety,
17 legislation, and cost of production. In order to analyze these and other issues, different models
18 have been proposed and used by the AWE community. There exist models for simulation purposes,
19 which include detailed system dynamics with a high complexity. Other models are designed for op-
20 timization, which are simplified appropriately and based on at least twice differentiable functions.
21 The models can be further distinguished by their mathematical formulation and the research focus
22 within AWE. In [6] a benchmark model of a soft wing is presented in polar coordinates for opti-
23 mization purposes. The focus is on the verification of the controller model, but it is not validated
24 against real data. In [7], different soft wing models are presented and compared. The models are
25 real-time oriented but no focus has been laid on the generated power output. In this paper the
26 focus is on a rigid wing model in pumping mode and an accurate power output computation, which
27 both is not given in previous work.

28 The proposed model uses a description in Cartesian coordinates [8] as opposed to polar coor-
29 dinates [9, 10], hence providing a formulation that is easier to handle for numerical optimization
30 tools. Tether models have been proposed for AWE systems in [7, 9, 11]. In the model proposed
31 here, we neglect any tether dynamics and consider the tether as a straight rigid link with a mass and
32 an aerodynamic drag. The wing dynamics are represented by the wing position, the translational
33 and rotational speed, the external forces and the orientation, where the orientation is supported
34 via rotation matrices, as proposed in [8].

35 A similar model formulation has been used in research [12, 13] and in the industry [11] where it
36 was used for optimizing the starting and landing of an AWE system. However, a validation of this
37 model is not available yet. In this paper, we validate this model as a tool for power optimization
38 using real flight data from the Ampyx Power prototype AP2 [2]. The parameters used in the model
39 are provided by the company, and are obtained by CFD analyses, several different test flights and
40 carefully performed measurements.

41 The validated model is described in detail in this paper, with the purpose of being reproduced
42 and utilized by other researchers, and hence, presents a reference model for research on AWE power
43 optimization. This paper is structured as follows. Section 2 describes the system dynamics and
44 the aerodynamical model in a detailed way. Section 3 presents the wing prototype AP2 and its
45 components, the aerodynamic coefficient determination and the method of comparing model and
46 measurement data. In section 4 the results are presented and discussed. In the last section the
47 conclusions are drawn.

48 2. Mathematical model

49 In this section the model dynamics of an AWE system in pumping mode is presented. The
50 system is in the form of differential algebraic equations (DAEs) [14]. The physical formulation of
51 the dynamics is an index-3 DAE based on Lagrange mechanics [15]. For an efficient application of
52 classical integration methods, an index reduction is performed by time differentiating the constraint

53 twice. This results in a fully implicit index-1 formulation of the dynamics [14] taking the form

$$\mathbf{0} = \mathbf{f}(\dot{\mathbf{x}}, \mathbf{x}, \mathbf{z}, \mathbf{u}) \quad (1)$$

54 where $\mathbf{f} : \mathbb{R}^{n_{\dot{x}}} \times \mathbb{R}^{n_x} \times \mathbb{R}^{n_z} \times \mathbb{R}^{n_u} \rightarrow \mathbb{R}^{n_x+n_z}$ and $\mathbf{x} \in \mathbb{R}^{n_x}$, $\mathbf{z} \in \mathbb{R}^{n_z}$ are respectively differential and algebraic states and $\mathbf{u} \in \mathbb{R}^{n_u}$ the control inputs.

56 Throughout the paper, if not a function, small case letters define scalars, bold small case letters present vectors and bold large case letters define matrices.

58

59 2.1. Reference frames

60 The system is modeled in Cartesian coordinates as done in [8, 13]. Compared to polar coordinates, as used in [10], the modeling in Cartesian coordinates yields less non-linear and less complex equations.

63 Two reference frames are defined. A fixed right-handed inertial reference frame \hat{n} placed at the attachment point of the tether to ground, with the basis vectors $[\hat{\mathbf{n}}_x, \hat{\mathbf{n}}_y, \hat{\mathbf{n}}_z]$, where $\hat{\mathbf{n}}_y$ is aligned with the main wind direction and $\hat{\mathbf{n}}_z$ is down. A second reference frame \hat{b} , labelled body frame, is attached to the wing with its origin at the Center of Mass (CoM). The orthogonal unit basis vectors $[\hat{\mathbf{e}}_x, \hat{\mathbf{e}}_y, \hat{\mathbf{e}}_z]$ of the body frame are defined such that $\hat{\mathbf{e}}_x$ points forward through the nose, $\hat{\mathbf{e}}_y$ points along the starboard wing, and $\hat{\mathbf{e}}_z$ points down. The reference frames are visualized in Fig. 1.

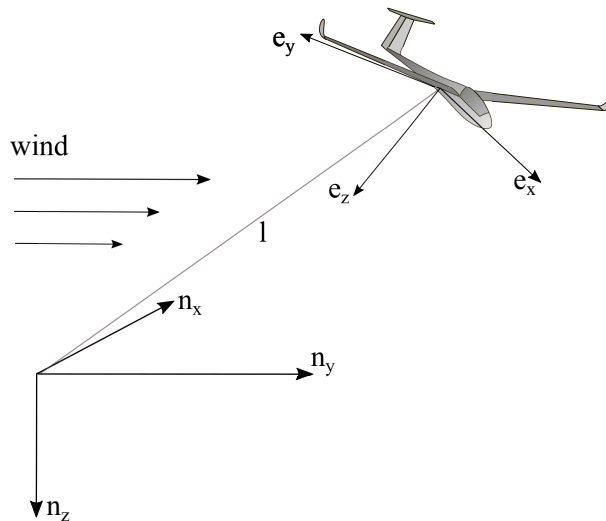


Figure 1: Coordinate system and vector conventions for the rigid-wing AWE system in pumping mode with the tether length l and wind in y direction.

69 *2.2. Model dynamics*

70 The wing is modeled as a one-point mass rigid body with 6 degrees of freedom (DOF) and a
 71 straight tether is assumed. The differential and algebraic states as well as control inputs are

$$\mathbf{x} = \begin{bmatrix} \mathbf{p} \\ \mathbf{v} \\ \mathbf{r} \\ \boldsymbol{\omega} \\ l \\ \dot{l} \\ \phi \end{bmatrix} \in \mathbb{R}^{23}, \quad \mathbf{z} = \lambda \in \mathbb{R} \quad \mathbf{u} = \begin{bmatrix} \dot{\phi} \\ \ddot{l} \end{bmatrix} \in \mathbb{R}^4, \quad (2)$$

72 where $\mathbf{p} \in \mathbb{R}^3$ is the CoM position in the inertial frame \hat{n} and $\mathbf{v} \in \mathbb{R}^3$ is the velocity of the
 73 CoM in frame \hat{n} . Vector $\mathbf{r} \in \mathbb{R}^9$ is a vector representation of matrix $\mathbf{R} \in \mathbb{R}^{3 \times 3}$, a direct cosine
 74 matrix (DCM), which transforms vectors expressed in \hat{n} to vectors expressed in \hat{b} . The reason
 75 for choosing the DCM representation is two-fold: (i) as the model is aimed at being used within
 76 numerical optimal control, it is preferable to use a non-singular representation of the rotations.
 77 Indeed, if using a minimal representation (such as e.g. Euler angles), it is difficult to ensure that
 78 the model trajectories will not pass through (or close to) the singularity during the iterations
 79 performed by the numerical solver. If some iterations come close to the singularity, the solver can
 80 fail for purely numerical reasons and hence not deliver a solution of the optimal control problem,
 81 (ii) the DCM representation yields models that are less nonlinear than other representations using
 82 less states than the DCM. In the context of numerical optimal control, models having less severe
 83 nonlinearities are preferred, as they tend to yield a faster and more reliable convergence of the
 84 numerical tools deployed for solving the optimal control problem.

85 Variable $\boldsymbol{\omega} \in \mathbb{R}^3$ is the angular velocity of the wing in frame \hat{b} . The variables $l, \dot{l}, \ddot{l} \in \mathbb{R}$ gather
 86 the tether components which are the tether length l , speed \dot{l} , and the acceleration \ddot{l} as control
 87 input. Variables $\phi \in \mathbb{R}^3, \dot{\phi} \in \mathbb{R}^3$ collect the control surface deflection aileron $\phi_a \in \mathbb{R}$, elevator
 88 $\phi_e \in \mathbb{R}$, and rudder $\phi_r \in \mathbb{R}$ as states and their time derivatives as control inputs.

89 The tether is assumed straight, and is represented in the model by the constraint

$$C = \frac{1}{2}(\mathbf{p}^\top \mathbf{p} - l^2) = 0, \quad (3)$$

90 stating that the CoM of the wing must be at a distance l of the attachment point of the tether
 91 to the ground. Finally, λ is the algebraic variable related to that constraint in Lagrange modeling
 92 [15], and is proportional to the tether tension.

93 Since (3) is *holonomic*, i.e. purely position-dependent, one has to differentiate it twice in order
 94 to obtain an index-1 DAE [14], i.e. we use

$$\dot{C} = \mathbf{v}^\top \mathbf{p} - l\dot{l} = 0 \quad (4a)$$

$$\ddot{C} = \dot{\mathbf{v}}^\top \mathbf{p} + \mathbf{v}^\top \mathbf{v} - \dot{l}^2 - l\ddot{l} = 0. \quad (4b)$$

95 The index reduced DAE then enforces (4b) at all time, and (3)-(4a) at an arbitrary point in
 96 time, e.g. $t = 0$.

97 The evolution of the position and orientation of the wing are then simply expressed as

$$\dot{\mathbf{p}} = \mathbf{v}, \quad \dot{\mathbf{R}} = \mathbf{R}\omega_{\times}, \quad (5)$$

98 where ω_{\times} is the skew symmetric matrix associated to the rotational velocity ω . In order to have
99 a valid DCM R , the orthonormality constraint

$$\mathbf{R}^{\top} \mathbf{R} - \mathbf{I} = 0 \quad (6)$$

100 must be imposed at an arbitrary point in time, e.g. $t = 0$.

The translational and rotational acceleration of the wing $\dot{\mathbf{v}}, \dot{\omega}$ are defined by the gravitational, tether, aerodynamic forces and moments acting on the wing. All forces act at the CoM of the wing. Gravitation is computed as $\mathbf{F}_g = m \cdot g \cdot \hat{\mathbf{n}}_z$, where m as the mass of the system and $g = 9.81\text{m/s}^2$. The drag and lift forces acting on the wing are combined in a single aerodynamic force \mathbf{F}_A . An additional drag $\mathbf{F}_{T\text{drag}}$ is created by the tether. The detailed aerodynamic model for computing \mathbf{F}_A and $\mathbf{F}_{T\text{drag}}$ is given in the section 2.3. The tether force acting on the wing reads as

$$\mathbf{F}_t = \lambda \mathbf{p}. \quad (7)$$

101 The sum of the forces yields the wing acceleration, i.e.

$$\dot{\mathbf{v}} = m^{-1} [\mathbf{F}_A + \mathbf{F}_g + \mathbf{F}_{T\text{drag}} + \mathbf{F}_t]. \quad (8)$$

102 The rotational acceleration $\dot{\omega}$ is purely related to the aerodynamic moments \mathbf{M}_A and reads as:

$$\dot{\omega} = \mathbf{J}^{-1} [\mathbf{M}_A - (\omega \times \mathbf{J} \cdot \omega)], \quad (9)$$

103 where \mathbf{J} is the inertia matrix of the wing in the body frame. The detailed computation of the
104 aerodynamic moments \mathbf{M}_A is explained in section 2.3.

105 Equations (4b), (5),(8), (9) result in the full system dynamics. The addition of the constraints
106 of (4a)|_{t=0}, (3)|_{t=0} and (6)|_{t=0} complete the dynamics of the AWE system. When implementing
107 this model in a power optimization problem, where a periodic optimization is solved, additional
108 care has to be taken in formulating and solving the problem, which is detailed in [13, 16, 17]. The
109 next section gives a detailed explanation of the aerodynamic model.

110 2.3. Aerodynamic model

111 The aerodynamic model contains the computation of the aerodynamic forces and moments,
112 which are nonlinear functions of the system states. The aerodynamic forces and moments interact
113 with the kinematics in a feedback fashion, as the forces and moments depend on the states and
114 influence their time evolution. This feedback loop makes the model dynamics highly complex and
115 unstable. The aerodynamics are similar to standard aircraft flight mechanics, but the presence of
116 the tether yields drastically different dynamics.

117 The wind acting on the system is given in the earth coordinate frame \hat{n} . The wind is commonly
118 approximated via the power law wind shear model [18], in which the wind has a constant direction
119 and its speed is a function of the altitude $h = -\mathbf{p}_3$. It is given by

$$\|\mathbf{w}\| = w_0 \left(-\frac{\mathbf{p}_3}{h_0} \right)^z, \quad (10)$$

where h_0 is a wind shear reference altitude, w_0 the wind magnitude at that reference altitude, and z a roughness coefficient representing the shear effect. Note, that $\mathbf{w} = [w_x, w_y, w_z]$ is a 3-dimensional vector and can hold also varying winds or wind profiles if a more detailed wind model is desired. Using wind \mathbf{w} the apparent velocity of the wing is given by

$$\mathbf{v}_a = \mathbf{v} - \mathbf{w} \quad (11)$$

120 in frame \hat{n} . It describes the actual wind flow the wing experiences during flight. The forces acting
121 on the wing dependent on the apparent speed are described as:

$$\mathbf{F}_A = \frac{1}{2} \rho \|\mathbf{v}_a\|^2 S (C_X \hat{\mathbf{e}}_x + C_Y \hat{\mathbf{e}}_y + C_Z \hat{\mathbf{e}}_z), \quad (12)$$

122 where S is the aerodynamic reference area corresponding to the projected surface area of the wing,
123 and ρ is the local air density.

124 The aerodynamic moment with coefficients C_l, C_m, C_n is defined similarly, though it is common
125 to express it in the body frame. It reads as:

$$\mathbf{M}_A = \frac{1}{2} \rho \|\mathbf{v}_a\|^2 S (b C_l \hat{\mathbf{e}}_x + c C_m \hat{\mathbf{e}}_y + b C_n \hat{\mathbf{e}}_z), \quad (13)$$

126 where b is the reference wingspan and c is the reference chord length of the wing. This aerodynamic
127 model is based on the assumption that the airflow around the wing settles instantaneously to its
128 steady-state, such that the aerodynamic forces and moments depend on the instantaneous state \mathbf{x}
129 of the airframe only.

130 The airflow direction is defined by the aerodynamic angle of attack α and sideslip angle β which
131 are expressed in radians in the body frame as:

$$\alpha = \arctan \left(\frac{\hat{\mathbf{e}}_z^\top \mathbf{v}_a}{\hat{\mathbf{e}}_x^\top \mathbf{v}_a} \right), \quad \beta = \frac{\hat{\mathbf{e}}_y^\top \mathbf{v}_a}{\hat{\mathbf{e}}_x^\top \mathbf{v}_a}. \quad (14)$$

132 These angles, together with the surface deflections ϕ , are needed in order to compute the
133 corresponding aerodynamic coefficients $C_{\{X,Y,Z\}}, C_{\{l,m,n\}}$ given by

$$\begin{aligned} \begin{bmatrix} C_X \\ C_Y \\ C_Z \end{bmatrix} &= \begin{bmatrix} C_{X0}(\alpha) \\ C_{Y0}(\alpha) \\ C_{Z0}(\alpha) \end{bmatrix} + \begin{bmatrix} C_{X\beta}(\alpha) \\ C_{Y\beta}(\alpha) \\ C_{Z\beta}(\alpha) \end{bmatrix} \beta \\ &+ \begin{bmatrix} C_{Xp}(\alpha) & C_{Xq}(\alpha) & C_{Xr}(\alpha) \\ C_{Yp}(\alpha) & C_{Yq}(\alpha) & C_{Yr}(\alpha) \\ C_{Zp}(\alpha) & C_{Zq}(\alpha) & C_{Zr}(\alpha) \end{bmatrix} \begin{bmatrix} b \omega_x \\ c \omega_y \\ b \omega_z \end{bmatrix} \frac{1}{2 \|\mathbf{v}_a\|} \\ &+ \sum_{i \in \{a,e,r\}} \begin{bmatrix} C_{X\phi_i}(\alpha) \phi_i \\ C_{Y\phi_i}(\alpha) \phi_i \\ C_{Z\phi_i}(\alpha) \phi_i \end{bmatrix}, \end{aligned} \quad (15)$$

and

$$\begin{aligned} \begin{bmatrix} C_l \\ C_m \\ C_n \end{bmatrix} &= \begin{bmatrix} C_{l0}(\alpha) \\ C_{m0}(\alpha) \\ C_{n0}(\alpha) \end{bmatrix} + \begin{bmatrix} C_{l\beta}(\alpha) \\ C_{m\beta}(\alpha) \\ C_{n\beta}(\alpha) \end{bmatrix} \beta \\ &+ \begin{bmatrix} C_{lp}(\alpha) & C_{lq}(\alpha) & C_{lr}(\alpha) \\ C_{mp}(\alpha) & C_{mq}(\alpha) & C_{mr}(\alpha) \\ C_{np}(\alpha) & C_{nq}(\alpha) & C_{nr}(\alpha) \end{bmatrix} \begin{bmatrix} b \omega_x \\ c \omega_y \\ b \omega_z \end{bmatrix} \frac{1}{2 \|\mathbf{v}_a\|} \\ &+ \sum_{i \in \{a,e,r\}} \begin{bmatrix} C_{l\phi_i}(\alpha) \phi_i \\ C_{m\phi_i}(\alpha) \phi_i \\ C_{n\phi_i}(\alpha) \phi_i \end{bmatrix} \end{aligned} \quad (16)$$

134 The aerodynamic coefficients $C_{\{X,Y,Z\}}, C_{\{l,m,n\}}$ are generally estimated via flight tests and presented
 135 as look-up tables in terms of the angle of attack α , the side slip β , and the surface controls ϕ .
 136 For modeling and optimization purposes these look-up tables need to be approximated by e.g.
 137 polynomials or spline functions. Such method is sufficiently accurate for attached flows at low
 138 angles of attack. In this paper the coefficients for the Ampyx wing AP2 are used, listed in Section
 139 3.1.

140 One of the main differences between a conventional and a tethered wing is the presence of the
 141 tether which induces additional drag, weight and possibly moments if the tether is not attached at
 142 the CoM of the wing. A model of the tether is crucial for an accurate AWE model. In this model
 143 it is assumed that the tether is attached at the CoM of the wing, such that drag does not generate
 144 moments in the wing dynamics. In [19] the drag force generated by the whole tether length is
 145 simplified in to

$$T_D = \frac{1}{8} \rho C_T d_{\text{tet}} l \|\mathbf{v}_a\|, \quad (17)$$

146 where C_T is the drag coefficient and d_{tet} the tether diameter. It is assumed that the drag is acting
 147 on the wing in the direction \mathbf{v}_a , which results in the tether drag, described in earth frame,

$$\mathbf{F}_{T\text{drag}} = -T_D \mathbf{v}_a. \quad (18)$$

148 Dynamics and constraints can be adjusted in order to include a refined tether model or adding e.g.
 149 a ground station representing the mechanical-electrical energy conversion.

150 3. Method

151 In this section, we present the Ampyx Power prototype (AP2) and the procedure deployed for
 152 obtaining the wing parameters and the real test flight data. We then explain the procedure of
 153 assessing the capability of the model to match the flight data.

154 3.1. Description of the AWE prototype

155 The Ampyx Power Prototype 2 (AP2) AWE system is a prototype built by the dutch company
 156 Ampyx Power B.V. in order to develop and test new control algorithms for AWE and push the
 157 technology towards its full automation [2]. First flown in 2009, the 30 kW system with 5.5 m
 158 wingspan comprises several years of development and technological progress and is, by the time of
 159 writing, one of the most advanced airborne wind energy systems in the world. The AP2 wing is
 160 displayed in Fig. 2. Because of the availability of data and parameters, and the willingness of the
 161 company to share flight information, this system is used in this work.

162 3.1.1. Physical components of the system

163 The AP2 system consists of a ground-based generator, a winch, a polyethylene tether, and a
 164 wing that also contains electrical components for the automatic control of the flight. Because the
 165 focus is laid on the validation of the flight model and the mechanical power output, the electrical
 166 details of the generator are omitted. The wing is controlled using classical control surfaces i.e.
 167 a rudder at the vertical stabilizer for yaw control, elevators at the horizontal stabilizer for pitch
 168 control, and ailerons at the wing for rolling maneuvers. The deflection of the control surfaces are
 169 measured and collected in vector $\hat{\phi} \in \mathbb{R}^3$. Flaps are only active during landing and are therefore
 170 not considered here.

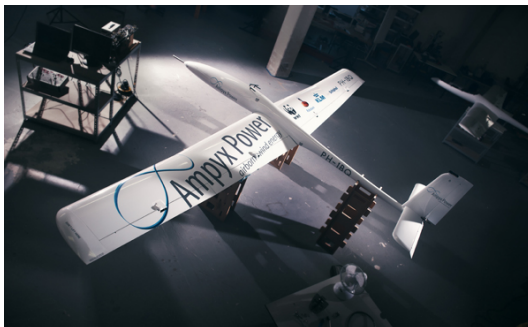


Figure 2: Ampyx Power prototype AP2 [2]. The flight data were collected during several test flights with this prototype.

171 The prototype is equipped with several sensors, installed in the winch and on the wing. The
 172 wing is equipped with a GPS sensor, IMU sensor, and a pitot tube. Using filter algorithms, this
 173 sensor information is fused to estimate the position $\hat{\mathbf{p}} \in \mathbb{R}^3$, velocity $\hat{\mathbf{v}} \in \mathbb{R}^3$, orientation $\hat{\mathbf{R}} \in \mathbb{R}^{3 \times 3}$,
 174 the rotational speed $\hat{\boldsymbol{\omega}} \in \mathbb{R}^3$, airspeed $\hat{v}_A \in \mathbb{R}^3$, the angle of attack $\hat{\alpha} \in \mathbb{R}$ and the angle of sideslip
 175 $\hat{\beta} \in \mathbb{R}$. The horizontal wind speed $\hat{\mathbf{w}} \in \mathbb{R}^2$ is estimated based on signals obtained from a 5-holes
 176 probe and the GPS velocity. At the winch the tether speed $\hat{l} \in \mathbb{R}$, tether acceleration $\hat{\dot{l}} \in \mathbb{R}$, and
 177 tether force $\hat{\mathbf{F}}_t = \lambda \|\mathbf{p}\| \in \mathbb{R}$ are estimated. This data are logged at a frequency of 50 Hz during
 178 each flight.

179 The flight model described in Section 2 depends on parameters that are specific for this pro-
 180 totype. The kinematic and geometric parameters are summarized in Table 1. The aerodynamic
 181 parameters are described in the next subsection.

Table 1: Kinematic and geometric system specifications of Ampyx wing AP2

parameter	value	description
S	3	wing area [m ²]
b	5.5	wing span [m]
c	0.55	wing chord [m]
m	36.8	weight [kg]
$J_{(xx,yy,zz,xz)}$	25, 32, 56, -0.47	inertia matrix [kg·m ²]
d_{tet}	0.0025	tether diameter [m]
ρ_t	0.0046	tether density [kg/m]
C_t	1.2	tether drag coefficient [-]
ρ	1.225	air density [kg/m ³]

182 3.1.2. Determination of the aerodynamic coefficients

The aerodynamic coefficients of the wing have been identified by Ampyx Power with the help of CFD analyses in AVL [20] and during several untethered test flights. During these flights short maneuvers were flown in which specific control inputs were given and the responses of the system were recorded. For each control surface, separate untethered test flights were executed to determine the aerodynamic coefficients individually whenever possible. The resulting coefficients C_{XYZ} and C_{lmn} for the aerodynamic forces and moments have then been represented as polynomial functions

of the angle of attack α . In Table 2 the polynomial coefficients are listed as $[c_2 \ c_1 \ c_0]$ such that the aerodynamic coefficients are obtained as

$$C_i = [c_2 \ c_1 \ c_0] \begin{bmatrix} \alpha^2 \\ \alpha \\ 1 \end{bmatrix}. \quad (19)$$

183 Parameters that are not listed are equal to zero.

Table 2: Dimensionless polynomial coefficients resulting in the aerodynamic coefficients which are implemented in the aerodynamic model (15) and (16), using convention (19).

C_X	Value	C_m	Value
C_{X_0}	[2.5549, 0.4784, -0.0293]	C_{m_0}	[0,-0.6027, -0.0307]
C_{X_q}	[0, 4.4124, -0.6029]	C_{m_q}	[5.2885,-0.0026,-11.3022]
$C_{X_{\phi_e}}$	[0, 0.1115,-0.0106]	$C_{m_{\phi_e}}$	[0.9974,-0.0061,-1.0427]
C_Y		C_l	
C_{Y_β}	[0.0936,-0.0299,-0.1855]	C_{l_β}	[0.0312,-0.0003,-0.0630]
C_{Y_p}	[0.0496,-0.0140,-0.1022]	C_{l_p}	[0.2813,-0.0247,-0.5632]
C_{Y_r}	[0,0.1368,0.1694]	C_{l_r}	[0,0.6448,0.1811]
$C_{Y_{\phi_a}}$	[0.0579,-0.0024,-0.0514]	$C_{l_{\phi_a}}$	[0.2383,-0.0087,-0.2489]
$C_{Y_{\phi_r}}$	[-0.1036,0.0268,0.10325]	$C_{l_{\phi_r}}$	[0,-0.0013,0.00436]
C_Z		C_n	
C_{Z_0}	[5.7736, -5.0676, -0.5526]	C_{n_β}	[0,-0.0849,0.0577]
C_{Z_q}	[6.1486,0.1251,-7.5560]	C_{n_p}	[0,-0.9137,-0.0565]
$C_{Z_{\phi_e}}$	[0.2923,-0.0013,-0.315]	C_{n_r}	[0.02570,0.0290,-0.0553]
		$C_{n_{\phi_a}}$	[0,-0.1147,0.01903]
		$C_{n_{\phi_r}}$	[0.04089,-0.0117,-0.0404]

184 3.2. Formulation of the validation problem

185 It is important to observe here that while physical parameters such as masses, inertias, lengths
186 and diameters are comparably easy to estimate accurately, the parameters underlying the aerody-
187 namic model are, in contrast, more difficult to estimate.

188 We propose to assess the model on the real data via performing a fitting of the model trajec-
189 tories to the measurements obtained during real flight experiments, i.e. a least squares problem
190 minimizing the difference between model and measurement data. This approach will allow us to
191 observe what parts of the model trajectories cannot accurately fit the real data, and identify what
192 parts of the model are the least accurate. The measurements to be fitted to the model are col-
193 lected in the data output vector $\hat{\mathbf{y}} = [\hat{\mathbf{p}}, \hat{\mathbf{v}}, \hat{\mathbf{R}}, \hat{\boldsymbol{\omega}}, \hat{l}, \hat{\mathbf{w}}, \hat{\boldsymbol{\phi}}]$ and the corresponding model output in
194 $\mathbf{y} = [\mathbf{p}, \mathbf{v}, \mathbf{R}, \boldsymbol{\omega}, l, \mathbf{w}, \boldsymbol{\phi}]$.

For the validation the wind speed \mathbf{w} is not modeled by the wind shear model (10), but the state $\mathbf{w} \in \mathbb{R}^2$ is introduced in the model, following the dynamics:

$$\dot{\mathbf{w}} = \mathbf{u}_{\mathbf{w}} \quad (20)$$

195 and \mathbf{w} is fitted to the wind data while $\mathbf{u}_{\mathbf{w}}$ is minimized using a square penalty. We therefore
196 assume that the wind can be described as a random walk driven by a Gaussian white noise.

The fitting problem minimizing the difference between measurement data and model can be formulated as

$$\begin{aligned} \min_{\mathbf{y}} & \int_0^{t_f} (\mathbf{y} - \hat{\mathbf{y}})^\top W_{\mathbf{y}} (\mathbf{y} - \hat{\mathbf{y}}) + W_{\mathbf{w}} \|\mathbf{u}_{\mathbf{w}}\|^2 dt & (21) \\ \text{s.t.} & (4b), (5), (8), (9), (3)|_{t=0}, (4a)|_{t=0}, (6)|_{t=0}, (20) \end{aligned}$$

197 The cost function in (21) penalizes the differences between the model output \mathbf{y} and measured data
 198 $\hat{\mathbf{y}}$. Matrix $\mathbf{W}_{\mathbf{y}}$ and scalar $W_{\mathbf{w}}$ should ideally hold the inverse of the covariance matrix of the
 199 measurement noises and wind rate of change. As this information is difficult to obtain, reasonable
 200 ad hoc values are chosen instead.

201 Problem (21) is solved numerically using the *direct collocation* method, which belongs to the
 202 family of direct optimal control methods [21]. The problem is discretized into a finite-dimensional
 203 NLP by splitting the state trajectories into 60 control intervals. Within each control interval the
 204 trajectories are represented by a Lagrange polynomial evaluated on the collocation points using a
 205 Radau scheme of degree 3 [22]. The Radau scheme is chosen due to its good numerical stability at
 206 the presence of DAEs [21, 22].

207 4. Results

208 In the previous section we described the method and tools we use in order to assess the model
 209 of the AWE system. In this section, the results of the fitting problem are shown and discussed.

210 4.1. Validation results

211 The method explained in Section 3 was used to assess the proposed model. The measurement
 212 data correspond to one pumping cycle that spans 50 s. One pumping cycle includes the reel-out
 213 of a single phase and the subsequent retraction phase. Several sequences of pumping cycles at
 214 different time points were extracted from the data for the validation procedure, resulting all in
 215 similar results. For the presentation of the results one cycle was selected.

216 The flight path during the actually flown power cycle is presented in Fig. 3.

217 The trajectory does not end exactly at the same position as the starting position because the
 218 flight controller does not enforce periodicity and the subsequent power orbit is slightly shifted. The
 219 small wings visualize the direction of flight and the red segments visualize the reel-in phase of the
 220 tether. The main wind direction is displayed as blue arrows in the plot.

221 Fig. 4 presents the position \mathbf{p} , ground speed \mathbf{v} and rotational speed $\boldsymbol{\omega}$ in the body frame on
 222 the left and the rotation matrix \mathbf{R} on the right.

223 The data is colored in solid grey, whereas the modeled variables are displayed in dashed green.
 224 The same color code is used throughout the whole result section. The plots in Fig. 4 present a
 225 good fit for all the variables. The measurements $\hat{\boldsymbol{\omega}}$ are noisy, while the trajectories of the modeled
 226 $\boldsymbol{\omega}$ are smoother compared to the data but follow the trend. The wind speed in the model and the
 227 original wind speed data is plotted in Fig. 5. The measurements contain only the horizontal wind
 228 components. It can be observed that due to the introduction of $\mathbf{u}_{\mathbf{w}}$ the wind trajectory, which
 229 is fed to the aerodynamic model is smoother than the actual measurement data. Variables $\|\mathbf{v}_{\mathbf{a}}\|$,
 230 α and β are displayed in Fig. 6. A mismatch between data and model of α and β is visible, but
 231 the general trend is adequate. The aerodynamic angles are generally difficult to measure which
 232 makes a mismatch likely. In Fig. 7 the surface deflections ϕ , aileron, elevator and rudder are

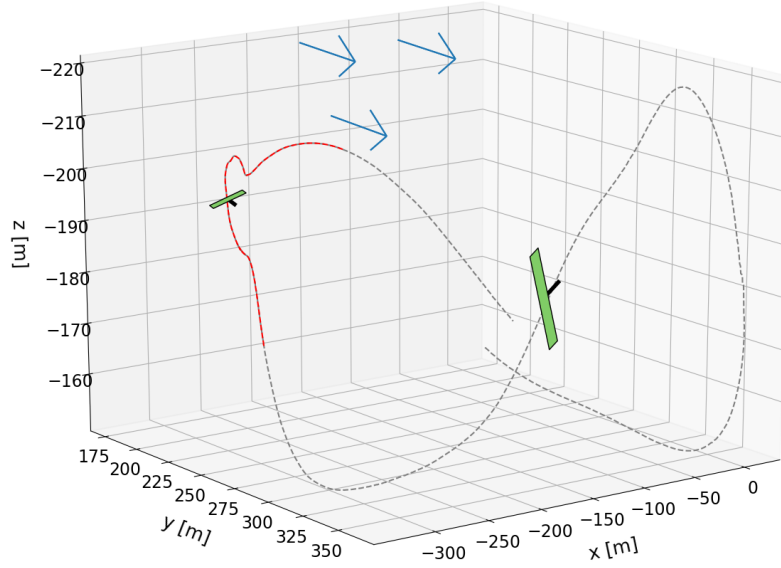


Figure 3: 3D plot of the fitted flight path of one pumping cycle, with the black small rod marking the tail of the wing. Red marked part defines the reel-in phase of the tether. The blue arrows label the wind direction.

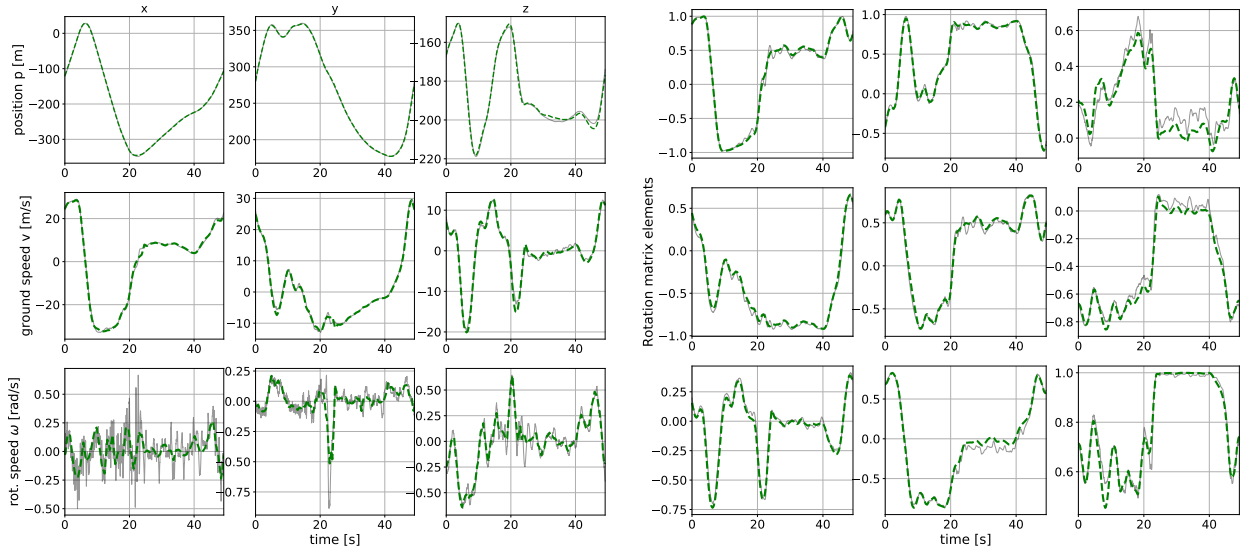


Figure 4: Left: Position \mathbf{p} [m], speed \mathbf{v} [m/s], angular velocity $\boldsymbol{\omega}$ [rad/s]. Right: rotation matrix \mathbf{R} . For both the data (solid grey) and model (dashed green) are shown. For all variables the model presents a good fit to the data.

233 displayed. One can observe an oscillation in the aileron in the first half of the data which does
 234 not appear the model. The modeled surface deflections are in general smoother than the data,
 235 but the trend of the trajectories fits well. In general, the model appears capable of fitting real
 236 tethered flight data regarding all variables including position, speed, rotation, angular velocities,
 237 aerodynamic angles, apparent speed and the surface deflections. From these results we conclude
 238 that kinematic, geometric, aerodynamic and lift and drag models are a fair representation of the

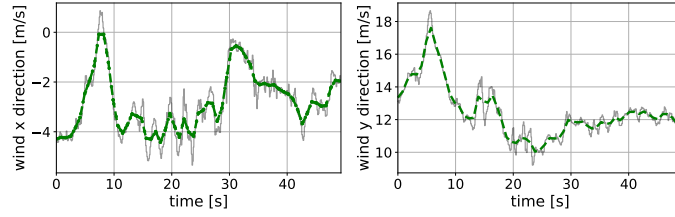


Figure 5: Wind variable \mathbf{w} fitted to wind measurements. Data in solid grey, model in dashed green.

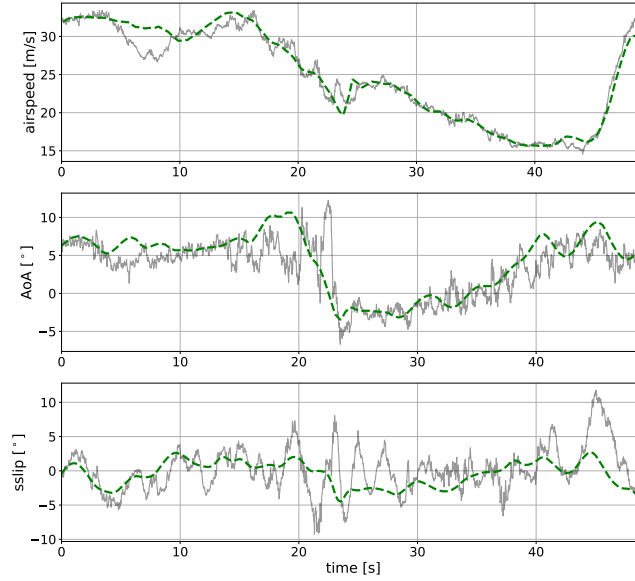


Figure 6: Apparent speed $\|\mathbf{v}_a\|$ [m/s], the angle of attack α [°] and the side slip β [°] follow the trend of the data. Measurement data in solid grey, model in dashed green. The aerodynamic angles are generally difficult to measure which is probably the reason for the slight mismatch. However, the general trend is adequate.

239 real system dynamics. In the next section, we assess the capability of the model at predicting the
 240 mechanical power extracted by the system.

241 4.2. Power output

242 The power output of the system is mainly defined by the tether speed and tether tension. Fig. 8
 243 (top) displays the tether reel-in and reel-out speed, both from the model and the measurements.
 244 The reel-out phase ($\dot{l} > 0$) generates power while the reel-in phase ($\dot{l} < 0$) consumes power. Fig. 8
 245 (top) shows a better fit of the tether speed during the reel-out phase than during the reel-in. The
 246 difference in fit might be due to the straight tether assumption in the model. Indeed, during
 247 the traction phase the tether is under high tension, i.e. the straight tether assumption in the
 248 model is fair. However, under lower tension, during the retraction phase, the tether is likely to
 249 sag more, resulting in a larger mismatch. The measured and modeled tether tension is displayed
 250 in Fig. 8 (bottom). The modeled tether tension is given by $\lambda\|\mathbf{p}\|$. During the high-tension phase,
 251 severe oscillations can be seen in the measurements, which are most likely caused by real tether
 252 oscillations. As the model does not incorporate tether elasticity, it can not capture such oscillations.
 253 In general the tether tension estimated by the model follows nonetheless decently well the average

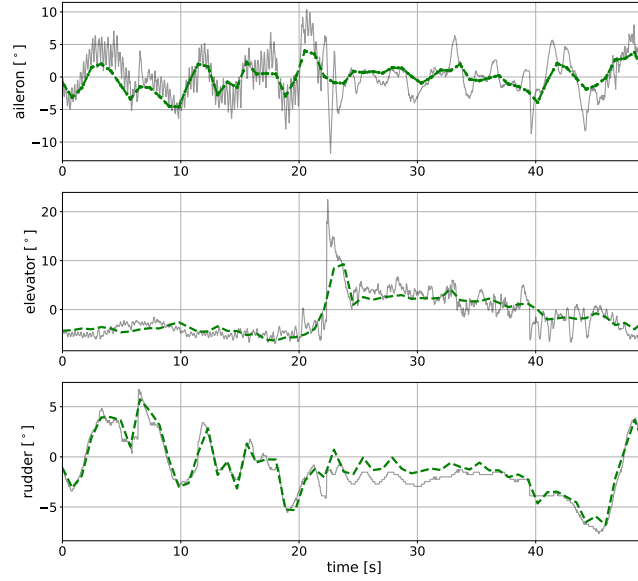


Figure 7: Control surface deflections ϕ [°] (aileron, elevator and rudder). Measurement data in solid grey, model in dashed green. The trajectory of the modeled surface deflections is smoother but follows the trend of the data.

measured tension.

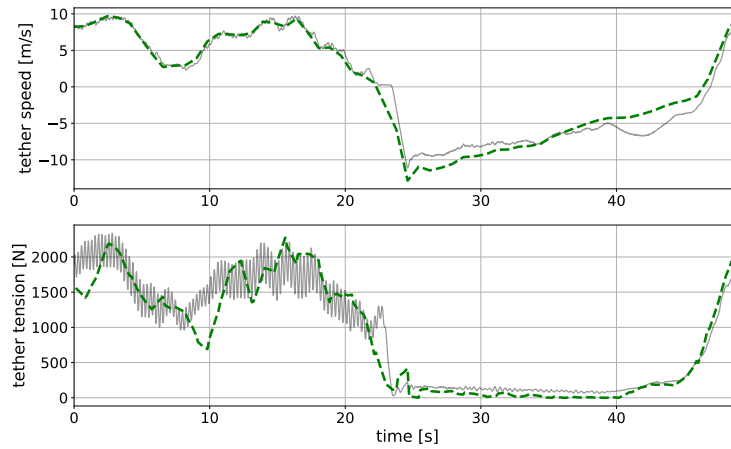


Figure 8: Top: tether speed (winch reel-in/-out speed) [m/s]. Bottom: tether tension in [N]. Measurement data in solid grey and model in dashed green. The visible oscillations in the measurements are most likely tether oscillations, which are however not captured in the model.

254

255 The good match is a quite striking observation provided that a simple straight tether model
 256 was used in this work. Hence, in the context of assessing power generation, the straight tether
 257 assumption appears justified.

258 The mechanical power output is computed in the model as $P_{mech} = \lambda \cdot \|\mathbf{p}\| \cdot \dot{i}$. In Fig. 9 the power
 259 output over the orbit is displayed. The actual mechanical power output is estimated by multiplying
 260 the measured tether speed and tether tension. The power needed to reel in the aircraft is a small
 261 fraction of the mechanical power extracted at the reel-out phase. The total energy production over

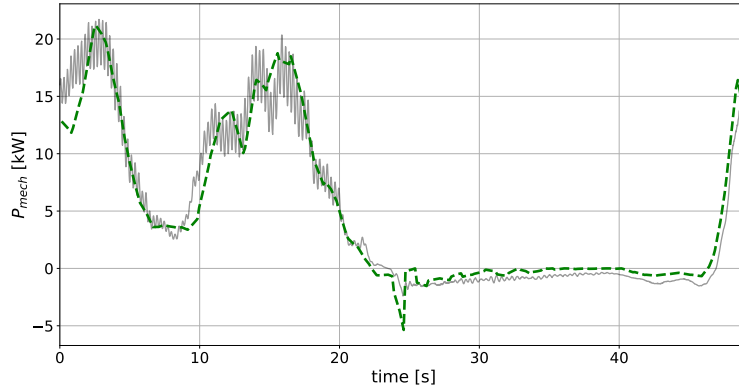


Figure 9: Mechanical power output [W] of one pumping cycle. Measurement data in solid grey and model in dashed green.

262 this pumping cycle is computed as the integral over the instantaneous power output. In the data
 263 the energy of one cycle is 66.52 Wh whereas the model estimates the energy to 67.32 Wh. The
 264 relative error is calculated as 1.2%.

265 This observation suggests that the tether oscillations observed in Fig. 8 do not dissipate a sig-
 266 nificant amount of energy, allowing the very good fit in the energy of the cycle under investigation.
 267 Hence, we assume that the tether oscillations are longitudinal in this prototype, and do not require
 268 the correction of an increased tether drag discussed in [23]. However, tether oscillations as the ones
 269 measured here arguably have a strong impact on component fatigue, and ought to be accounted
 270 for at the mechanical design phase.

271 The model was tested against multiple data sets and showed for all similarly good results. The
 272 different data sets were collected during a stable flight session at average wind conditions. For
 273 a more general assessment of the model, data should be collected during flights at low and high
 274 wind speeds and tested against the model. This limits the validity of the proposed model to power
 275 production cycles during average wind conditions.

276 5. Conclusion

277 In this paper a reference model of an airborne wind energy system in pumping mode was detailed
 278 and validated against real flight data of the a prototype wing AP2 of Ampyx Power. The validation
 279 was performed via a least squares fitting problem of the model state trajectories to complete flight
 280 data (position, speed, rotation, angular velocity, apparent wind speed and aerodynamic angles).
 281 The time horizon of the fitting was a single pumping cycle of 50s, comprising a reel-out and reel-
 282 in phase. The observations drawn on fitting this pumping cycle appeared consistent throughout
 283 the pumping cycles available in the dataset. It appears that the proposed model is capable of
 284 explaining very well the data obtained in the real system. The proposed model appeared fairly
 285 accurate at predicting the average power output of the system.

286 The tether speed and resulting mechanical power output are very close fit to the measurement
 287 with a relative error in output power of 1.2% . The tether tension of the model fits the data fairly
 288 well with some mismatch at specific times. Thus, we conclude that the assumption of a straight
 289 tether is an appropriate model choice in the context of power generation estimation. Despite
 290 the assumptions and simplifications proposed, the model presented is capable of explaining the

291 real data obtained in the AWE prototype developed by Ampyx Power and thus presents a valid
292 reference model for research related to power generation within AWE at average wind conditions.
293 Future work ought to test the model for flights during more extreme wind conditions in order to
294 assess its general validity.

295 Acknowledgment

296 This project has received funding from the European Union’s Horizon 2020 research and inno-
297 vation program under the Marie Skłodowska-Curie grant agreement No 642682. Disclaimer: This
298 document reflects only the authors’ view. The Commission is not responsible for any use that may
299 be made of the information it contains.

300 References

- 301 [1] A. Cherubini, A. Papini, R. Verthey, and M. Fontana, “Airborne wind energy systems: A review of the
302 technologies,” *Renewable and Sustainable Energy Reviews*, vol. 51, pp. 1461 – 1476, 2015.
- 303 [2] *Ampyx Power*, Available at <https://www.ampyxpower.com>, 2017.
- 304 [3] (2018). [Online]. Available: <https://x.company/makani/>
- 305 [4] (2018). [Online]. Available: <http://twingtec.ch>
- 306 [5] [Online]. Available: <http://awesco.eu>
- 307 [6] S. Costello, G. François, and D. Bonvin, “Crosswind kite control – a benchmark problem for advanced control
308 and dynamic optimization,” *European Journal of Control*, vol. 35, pp. 1 – 10, 2017.
- 309 [7] U. Fechner, R. van der Vlugt, E. Schreuder, and R. Schmehl, “Dynamic model of a pumping kite power system,”
310 *Renewable Energy*, vol. 83, pp. 705–716, 2015.
- 311 [8] S. Gros and M. Diehl, *Modeling of Airborne Wind Energy Systems in Natural Coordinates*. Berlin, Heidelberg:
312 Springer Berlin Heidelberg, 2013, pp. 181–203.
- 313 [9] P. Williams, B. Lansdorp, and W. Ockels, “Modeling and control of a kite on a variable length flexible inelastic
314 tether,” vol. 2, 08 2007.
- 315 [10] L. Fagiano, M. Milanese, and D. D. Piga, “Optimization of airborne wind energy generators,” *International*
316 *Journal of Robust and Nonlinear Control*, vol. 22, no. 18, pp. 2055–2083, 2012.
- 317 [11] J. Koenemann, P. Williams, S. Sieberling, and M. Diehl, “Modeling of an airborne wind energy system with
318 a flexible tether model for the optimization of landing trajectories,” *IFAC-PapersOnLine*, vol. 50, no. 1, pp.
319 11 944 – 11 950, 2017, 20th IFAC World Congress.
- 320 [12] G. Licitra, J. Koenemann, P. Williams, R. Ruiterkamp, G. Horn, and M. Diehl, “Viability assessment of a
321 rigid wing airborne wind energy pumping system.” in *Proceedings of the 2017 21st International Conference on*
322 *Process Control, PC 2017*, no. Proceedings of the 2017 21st International Conference on Process Control, PC
323 2017, Ampyx Power B.V, 2017, pp. 452–458.
- 324 [13] G. Horn, S. Gros, and M. Diehl, *Numerical Trajectory Optimization for Airborne Wind Energy Systems Described*
325 *by High Fidelity Aircraft Models*. Berlin, Heidelberg: Springer Berlin Heidelberg, 2013, pp. 205–218.
- 326 [14] U. M. Ascher and L. R. Petzold, *Computer methods for ordinary differential equations and differential-algebraic*
327 *equations*. Philadelphia: Society for Industrial and Applied Mathematics, 1998.
- 328 [15] A. J. Brizard, *An introduction to Lagrangian Mechanics*. World Scientific, 2015.
- 329 [16] S. Gros and M. Zanon, “Numerical optimal control with periodicity constraints in the presence of invariants,”
330 *IEEE Transactions on Automatic Control*, vol. 63, no. 9, pp. 2818–2832, 2017.
- 331 [17] S. Gros, M. Zanon, and M. Diehl, “A relaxation strategy for the optimization of airborne wind energy systems,”
332 in *2013 European Control Conference (ECC)*, July 2013, pp. 1011–1016.
- 333 [18] L. Landberg, *Meteorology for wind energy: an introduction*, 1st ed. Wiley, 2016.
- 334 [19] I. Argatov and S. Risto, *Efficiency of Traction Power Conversion Based on Crosswind Motion*. Springer Berlin
335 Heidelberg, 2013, pp. 205–218.
- 336 [20] [Online]. Available: <https://www.avl.com/fire>
- 337 [21] L. T. Biegler, “An overview of simultaneous strategies for dynamic optimization,” *Chemical Engineering and*
338 *Processing: Process Intensification*, vol. 46, no. 11, pp. 1043 – 1053, 2007, special Issue on Process Optimization
339 and Control in Chemical Engineering and Processing.

- 340 [22] L. T. Biegler,, “Nonlinear programming strategies for dynamic chemical process optimization,” *Theoretical*
341 *Foundations of Chemical Engineering*, vol. 48, no. 5, pp. 541–554, Sep 2014.
- 342 [23] S. Dunker, *Tether and Bridle Line Drag in Airborne Wind Energy Applications*. Springer Singapore, 2018, pp.
343 29–56.